01 Apr 2022

A Compact High-Isolation Wideband Three-Sector Linear Array

Sheng Wu

Lidong Chi

Fuhai Li

Francesco De Paulis

et. al. For a complete list of authors, see https://scholarsmine.mst.edu/ele_comeng_facwork/4650

Recommended Citation

S. Wu et al., "A Compact High-Isolation Wideband Three-Sector Linear Array," *IEEE Transactions on Antennas and Propagation*, vol. 70, no. 4, pp. 3094 - 3099, Institute of Electrical and Electronics Engineers, Apr 2022.

The definitive version is available at https://doi.org/10.1109/TAP.2021.3137421

Communication

A Compact High-Isolation Wideband Three-Sector Linear Array

Sheng Wu, Lidong Chi, Fuhai Li, Francesco de Paulis, and Yihong Qi

***Abstract*— A compact and highly isolated three-sector linear array is proposed targeting point-to-point or point-to-multipoint data communication in Central Business District (CBD) and residential subdivision applications. It features wide bandwidth, high isolation among the units, low wind load, and low manufacturing and installation costs within the 400–500 MHz band. The driving element of the array unit is a wideband high-efficiency electromagnetic structure (WHEMS) applied in combination with the metal rods as passive elements for isolation purposes. The parasitic rod, shared by the adjacent units, decouples the mutual coupling by reducing the distance, which realizes not only the high isolation capability but also reduced size. The beamwidth and the front-to-back ratio of the antenna are controlled by the combined effect of the metal rods and the bent of the active element. The impedance bandwidth of the antenna is 380–670 MHz (55%), and the H-plane half-power beamwidth (HPBW) is more than 70° in the 380–520 MHz. The front-to-back ratio is more than 19 dB and the gain is 8.2 ± 0.4 dBi in 400–500 MHz. The isolation is greater than 36 dB with unit spacing less than 0.2λ in 380–670 MHz.**

***Index Terms*— Array, common metal rods, compact, high isolation.**

I. Introduction

With the rapid development of long-term evolution (LTE) and 5G, people are demanding higher communication quality and speed, thus the Global System for Mobile Communications (GSM) technology may be soon abandoned. As a consequence, the 400 MHz GSM working band will become an idle band. Compared with the millimeter-wave bands, the 400 MHz GSM frequency range has the advantages of low attenuation, strong diffraction ability, and long propagation distance. The Third Generation Partnership Project (3GPP) has specified the GSM 450 MHz as the band 31 for LTE [1], which can be used for broadband communication in suburban and rural areas and for wireless communication in smart grids [2], [3]. In IoT applications, ISM 433 MHz is used for long-range radio (LoRa) technology [4], [5]. In the future, the 400–500 MHz interval will still play an important role in LTE, IoT, and even 5G applications.

There are applications of vertically polarized antennas in outdoor signal coverage and wireless data transmission [6]–[8]. The main application scenarios include point-to-point or point-to-multipoint data communication in Central Business District (CBD) and residential subdivision applications. The electrical size of the antenna is relatively large in this frequency band, thus it should be maintained as small as possible for applications in densely populated urban areas for reducing its visual impact and for maintenance considerations. The mutual coupling between units is an important aspect that needs to be solved for keeping low the overall antenna profile while achieving a reasonable isolation level among the array units. In suburban areas, larger unit spacing means larger towers to support the antenna.

Mutual coupling induced in the radiating element can severely degrade the output signal-to-noise ratio of the adaptive array antenna and the convergence of the array signal processing algorithms [9]. Mutual coupling in transmitter array antennas affects not only the radiated power but also the power receiving capability [10]. Such coupling cannot be reduced by increasing the distance among units due to space constraints. The reduction of the coupling current and the improvement of the port isolation are of great importance in antenna arrays for achieving a compact structure. The work in [11] compensated the existing coupling by connecting the antennas through neutralization lines in order to reduce the coupling problem of dual antenna units. Etched slits [12] and isolation slots [13] are also used to suppress surface waves on the ground plane, whereas an electromagnetic bandgap (EBG) substrate helps to reduce the coupling by reducing surface waves on the thick substrate of the microstrip antenna. In [14] and [15], a decoupling network is designed to connect the two ports for improving the port isolation. Moreover, with the development of massive multiple-input–multiple-output (MIMO) technologies, additional techniques are proposed such as the one in [16] where array-antenna decoupling surfaces (ADSs) are implemented to solve the decoupling problem of large array antennas, where ADS relies on the diffracted wave cancellation to minimize the coupling waves. So far, most of the decoupling techniques require the design of a separate decoupling structure.

Recently a directional antenna, based on a wideband high-efficiency electromagnetic structure (WHEMS), has been proposed as the driving element [17]–[22]; it achieves a wideband high gain with good radiation performance, thus being suitable for LTE and IoT applications [18], [19]. Moreover, it is suitable for base station applications since it is able to reduce wind resistance making advantage of metal rod reflectors instead of planar reflectors. The directional antenna for Wi-Fi dual-band proposed by Chi *et al.* [20] achieves a consistent H-plane dual-band beamwidth and, in the operating band, the antenna has a stable H-plane beamwidth of 66°–71°, which can be used for Wi-Fi applications. However, the design employs a metal reflector plate and a bent slot-loop antenna to control the beamwidth, and it is not used within an array. Therefore, the work in [20], although in principle it is suitable for designing array antennas, it has the disadvantages of using a metal plate reflector that increases the wind load of the antenna. Moreover, the induced currents generated on its surface also decrease the isolation of the antenna when applied within an array design.

In this communication, a linear array with compact structure, high isolation, and wide bandwidth from 400 to 500 MHz is proposed to be suitable for point-to-point or point-to-multipoint data communications. Moreover, the proposed WHEMS driving element, together with the decoupling solution offers the potential to design parasitic

Manuscript received April 6, 2021; revised September 14, 2021; accepted October 6, 2021. Date of publication December 29, 2021; date of current version April 7, 2022. *(Corresponding author: Yihong Qi.)*

Sheng Wu, Lidong Chi, and Fuhai Li are with the College of Electric and Information, Hunan University, Changsha 410082, China (e-mail: 1801793405@qq.com; 565548254@qq.com; fuhaili@vip.sina.com).

Francesco de Paulis is with the UAq EMC Laboratory, Department of Industrial and Information Engineering and Economics, University of L'Aquila, 67100 L'Aquila, Italy (e-mail: francesco.depaulis@univaq.it).

Yihong Qi is with the Peng Cheng Laboratory, Shenzhen 518066, China, also with LinkE Technology, Hengqin, Guangdong 519000, China, also with the College of Electric and Information, Hunan University, Changsha, China, also with the Electromagnetic Compatibility Laboratory, Department of Electrical and Computer Engineering, Missouri University of Science and Technology, Rolla, MO 65409 USA, and also with the School of Engineering, Western University, London, ON N6A 3K7, Canada (e-mail: yihong.qi@dbjtech.com).

Color versions of one or more figures in this communication are available at https://doi.org/10.1109/TAP.2021.3137421.

Digital Object Identifier 10.1109/TAP.2021.3137421

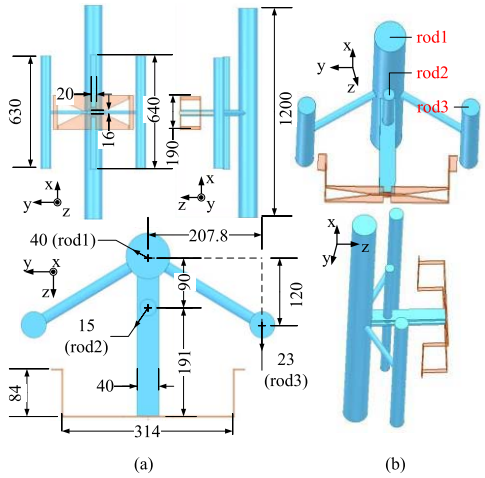

Fig. 1. Proposed antenna unit (with support rod). (a) Dimensions are in mm. (b) Three-dimensional model.

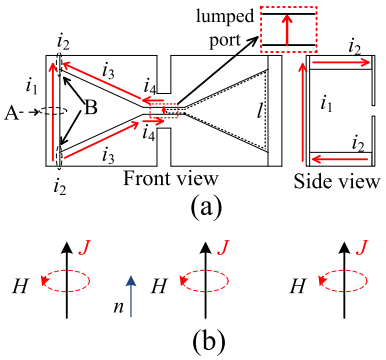

Fig. 2. Current analysis. (a) Current model. (b) Current equivalent model.

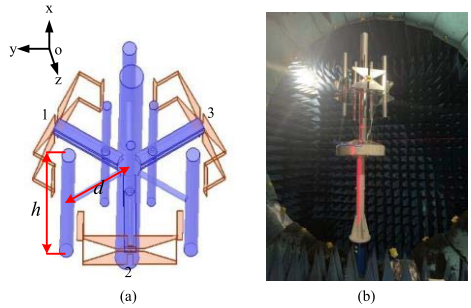

Fig. 3. Sector array. (a) Model for simulation. (b) Physical model.

elements that can be used for dual-polarization decoupling to achieve a compact design also for dual-polarization base station antennas. The proposed design requires encapsulating in a waterproof housing only the WHEMS, thus it offers low wind load compared to other designs [20]. The beamwidth and front-to-back ratio of the units are controlled by the structure of metal rods and by a bent slot-loop antenna. The bent driving element not only reduces the size of the antenna, but also reduces the distance from the reflector to the driving element itself. By keeping in mind the objective of a compact design, the reflector spacing of adjacent units tends to reduce, thus each radiator affects the radiation patterns of adjacent units. To overcome this limitation, a design scheme based on common metal rods is proposed. The common metal rod and the two adjacent units have a small spacing with strong mutual coupling, which can regulate the coupling current on each array unit and achieve decoupling. This scheme not only reduces the coupling between units, but also reduces the number of required metal rods, thus allowing more efficient element utilization than other decoupling methods.

In Section II, the design method of the array unit is introduced to describe the current model of the driving element and the role of the voltage balun. In Section III, the array design principle is introduced, and the decoupling principle of shared metal rods is analyzed in detail and verified by parametric analysis. In Section IV, simulated and measured results are analyzed to compare the performance of this design with other sector antennas. In Section V, a summary is presented.

II. Antenna Unit

The array unit is mainly composed of four parts: the radiating element made by the folded structure, metal rods, the balun, and the coaxial line, whose radius in mm is shown in Fig. 1. The thickness of the folded planar element is 2 mm, whereas the radius of the metal rod reflectors is 23 mm for rod1, 15 mm for rod2, and 40 mm for rod3.

The current of the driving element is abstracted and its current distribution in the left half is shown in Fig. 2(a), where i_2 indicates the current on the folded portion of the structure of length l_2, l_1 is the length of i_1, l_3 is the length of i_3, and l_4 is the length of i_4. The total length $l = l_1 + 2 \cdot l_2 + 2 \cdot l_3 + 2 \cdot l_4$ denotes the perimeter on both sides of the slot. The lengths $l_1 = 0.225\lambda$, $l_2 = 0.123\lambda$, $l_3 = 0.194\lambda$, and $l_4 = 0.068\lambda$ are calculated at 450 MHz. In order to reduce the impact of the bend, the point B of the bend should be near the minimum point of the current. Thus, the sum of l_1 and two times of l_2 provides a total length of almost half wavelength, and l is almost one wavelength, such that the current is zero at point B. The current can be decomposed to obtain the equivalent radiating model as shown in Fig. 2(b) [20]. According to this equivalent model, the radiating structure can be simply analyzed as three parallel dipoles. The metal rod reflector has a relevant reflection effect on the dipoles such that three vertical rods rod1, rod2, and rod3 are used to tune the radiation performance of the antenna. Among them, rod1 is the main mechanical support structure, since it employs a metal rod with a large radius; from an EM point of view, it acts mainly at reflecting the field generated by the current in the middle part of the antenna.

Both rod1 and rod2 have the effect of suppressing the back lobe, where rod2 is part of the antenna unit. Rod3 is located on both sides of the antenna unit, reflecting the field generated by the current on both folded sides of the driving element. All reflecting rods and the length of the folded portion of the radiating structure bend can be adjusted to tune the beamwidth and the front-to-back ratio of the overall antenna.

This design uses a coaxial line for feeding the radiating structure; there will be a non-zero current flowing on the outer surface of the coaxial line outer shield, which leads to an unbalanced feeding point and, as a consequence, such common-mode current affects the radiation performance of the antenna. A voltage balun can reduce the unbalanced current, thus it is included in the design.

III. Arrays and Decoupling

A. Array Design

The antenna unit proposed and described in Section II is employed to realize a linear array of three units, as the one shown in Fig. 3(a). Aluminum alloy is used for the antenna structure to reduce the weight of the overall array antenna. The physical model is fabricated by cutting, bending, and welding all-metal structures that make up the

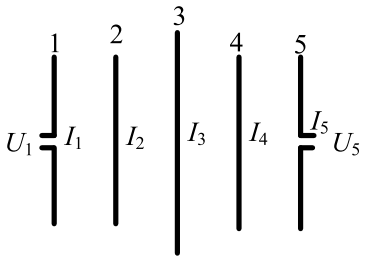

Fig. 4. Decoupling schematic.

array. The last welding step is preferred with respect to screwing to maximize the strength of the overall structure and avoid any additional metal parts that may affect the radiation performance. By bending the driving element, the dimension in the XOY plane can be reduced, thus a more compact structure can be achieved. The manufactured array, when placed inside the measurement chamber, is shown in Fig. 3(b). When the three radiating units are mounted together to realize the array, the limited horizontal spacing among the units introduces a detrimental effect on the radiation performances of each unit due to the mutual coupling. Moreover, the metal rods also affect the radiation performance of the adjacent units. In order to achieve a compact design, and to minimize the coupling effect among the three units, the design is refined by employing common metal rods between adjacent units, also targeting a reduction of the total number of metal rods. The coupling current on the common metal rods affects both adjacent units; however, such coupling current on the metal rods can be used to suppress the coupling current between two units, thus improving the isolation between adjacent array elements.

B. Decoupling Principle

The smaller the spacing, the larger the mutual coupling of units will be, with the current coupling being mainly generated by the adjacent units. The active structure in each array element is symmetric, and its current distribution is also symmetric, thus only the current coupling of one adjacent unit will be analyzed herein. According to the equivalent model in Fig. 2(b) of the radiating structure in Fig. 2(a), half of the unit can be modeled by a dipole and its parasitic element, as shown in Fig. 4, where dipoles 1 and 2 represent the right half of a left unit, dipoles 4 and 5 represent the left half of the antenna on its adjacent (right) unit, and 3 represents the common metal rod. The currents I_1 and I_2 satisfy (1), whereas currents I_4 and I_5 satisfy (2), according to [18]

$$I_2 = I_1 / \cos\left(\omega \cdot \frac{1}{2}\right) \tag{1}$$

$$I_4 = I_5 \cos\left(\omega \cdot \frac{1}{2}\right). \tag{2}$$

The calculation of the mutual impedance enables a qualitative analysis of the coupling current. The impedance equation is established by combining the current and impedance as in (3), where Z_{ii} denotes the self-impedance of the ith element, Z_{ij} denotes the mutual impedance between the ith element and the jth element. I_{i} denotes the current in the ith element, U_1 is the excitation voltage of element 1, and U_5 is the excitation voltage of element 5.

The relationship between I_1 and I_5 is obtained by simplifying (1) and (2) into (3), as shown at the bottom of the page, as in (4), shown at the bottom of the page. I_1 and I_5 interact with each other through the self-impedance and mutual impedance of the antenna unit and the common metal rod. From (4), it can be seen that the parameters Z_{33} and Z_{23} associated with the common metal rod become important factors affecting I_1 and I_5. Adjusting the length of the common metal rod can change the self-impedance Z_{33}, and adjusting the distance between the metal rod and the antenna can change the mutual impedances $Z_{\mathrm{i}3}$ and $Z_{3\mathrm{i}}$. For sake of brevity, by considering only the effect of I_1 on I_3, the expressions of I_3 as function of I_1 is shown in (5) where τ_m is the phase of mutual impedance and τ_θ is the phase of self-impedance [23]. The phase of I_3 is the function of both τ_m and τ_θ. By adjusting the length h of the common metal rod, the phase term τ_θ of the self-impedance can be modified; whereas the phase τ_m of the mutual impedance can be adjusted by varying the distance d, according to Fig. 3(a). The definition $\xi = \pi - \tau_m + \tau_\theta$ can be used to better highlight the impact of the common rod. When $\xi > 0$, the phase of I_3 exceeds that of I_1 and the common metal rod behaves as a reflector. The fields generated by I_1 and I_3 are inverted on adjacent units, thus the coupling becomes weaker, and the isolation is enhanced. However, when $\xi > 0$, the phase of I_3 lags behind that of I_1, thus the common metal rod behaves like a director. The fields generated by I_1 and I_3 are isotropic on adjacent units, thus leading to enhanced coupling and reduced isolation. The parametric study of the length h and the spacing d of the common metal rods described in the next paragraph help to optimize the design by maximizing the obtained decoupling level for the specific band of interest. However, when the length of the parasitic element is greater than 0.5λ, it is inductive and acts as a reflector; when its length is less than 0.5λ, it is capacitive and acts as a director. Rod1, rod2, and rod3 all need to behave as reflectors, so their lengths need to be greater than one-half wavelength. At a final design stage, their specific lengths can be further optimized to meet the target specs

$$I_3 = -\frac{I_1 Z_{13}}{Z_{33}} = -I_1 \frac{|Z_{13}|\, e^{j\tau_{\mathrm{m}}}}{|Z_{33}|\, e^{j\tau_\theta}} = I_1 \frac{|Z_{13}|}{|Z_{33}|} e^{j(\pi - \tau_{\mathrm{m}} + \tau_\theta)}. \tag{5}$$

C. Parametric Study

According to the decoupling principle of the common metal rod, the parameters d and h are important parameters that can be tuned accordingly to minimize the coupling, where h denotes the length of rod3, and d denotes the distance between the centers of rod3 and rod1. A parameter analysis is carried out to investigate the effects of these two factors, h and d, on the isolation between units of the

$$\begin{bmatrix} U_1 \\ 0 \\ 0 \\ 0 \\ U_5 \end{bmatrix} = \begin{bmatrix} Z_{11} & Z_{12} & Z_{13} & Z_{14} & Z_{15} \\ Z_{21} & Z_{22} & Z_{23} & Z_{24} & Z_{25} \\ Z_{31} & Z_{32} & Z_{33} & Z_{34} & Z_{35} \\ Z_{41} & Z_{42} & Z_{43} & Z_{44} & Z_{45} \\ Z_{51} & Z_{52} & Z_{53} & Z_{54} & Z_{55} \end{bmatrix} \begin{bmatrix} I_1 \\ I_2 \\ I_3 \\ I_4 \\ I_5 \end{bmatrix} \tag{3}$$

$$I_5 = I_1 \frac{Z_{33}\left[Z_{21} + Z_{22}\cos^{-1}(\omega \cdot l/2)\right] - Z_{23}\left[Z_{31} + Z_{32}\cos^{-1}(\omega \cdot l/2)\right]}{Z_{23}\left[Z_{35} + Z_{34}\cos(\omega \cdot l/2)\right] - Z_{33}\left[Z_{25} + Z_{24}\cos(\omega \cdot l/2)\right]} \tag{4}$$

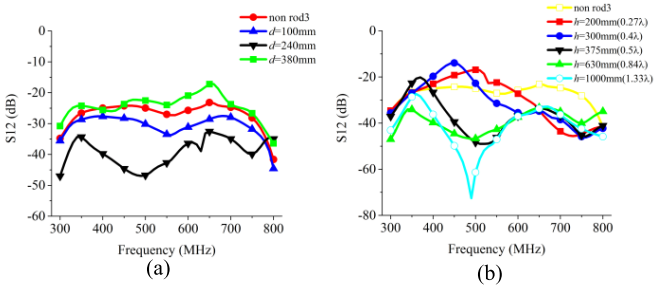

Fig. 5. Isolation. (a) S_{12} when rod3 is not present and d is 100, 240, and 380 mm ($h = 630$ mm). (b) S_{12} when h of rod3 is 0, 200, 300, 375, 630, and 1000 mm ($d = 240$ mm).

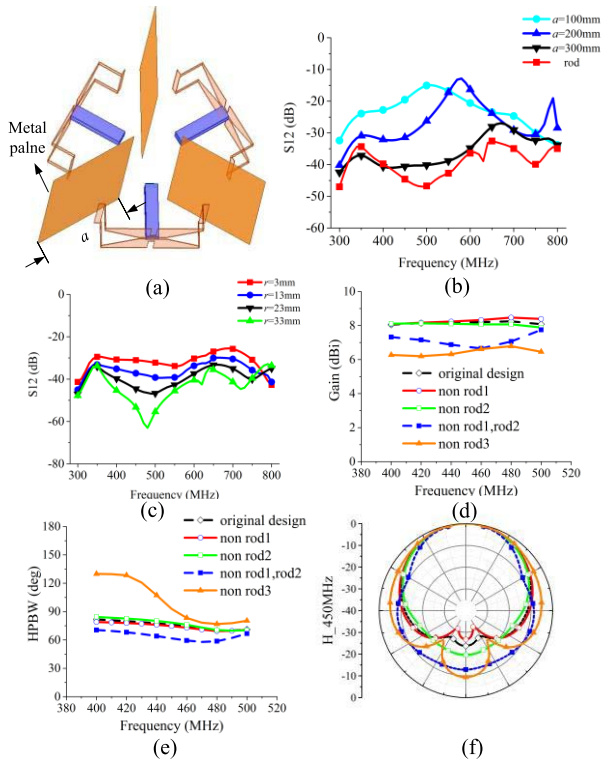

Fig. 6. Array with metal plane. (a) Model. (b) Isolation. (c) Analysis of rod radius. Rod analysis; (d) gain; (e) HPBW; (f) radiation pattern at 450 MHz.

array. The S-parameters between the excitation port of units 1 and 2 are shown in Fig. 5(a) and (b). In Fig. 5(a), the value $h = 630$ mm is kept fixed while varying d, whereas the analysis shown in Fig. 5(b) sets $d = 240$ mm and a variable h. When rod3 does not exist, the antenna isolation is greater than -25 dB; when $l = 630$ mm and $d = 240$ mm, the antenna isolation is greater than 36 dB, with the isolation being greater than 40 dB in the 400–500 MHz. When d is too small, its effect due to the mutual impedance between the units is too small, thus the effect on the coupling is small.

As shown in Fig. 6(a), metal planes of the same length are used instead of the common metal rod while removing other metal rods to further investigate the isolation effect of the metal rod structure. The width a of the metal plane is parametrically studied as shown in Fig. 6(b). The isolation effect of the metal rod structure can be achieved when a is greater than 300 mm, and its width is 6.5 times of the rod3. When a is equal to 100 mm, the isolation level is only

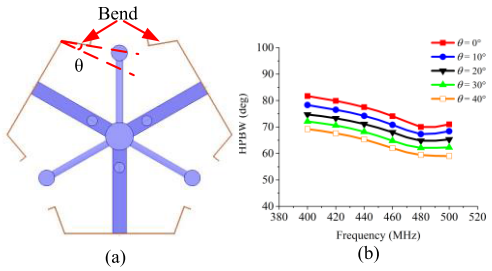

Fig. 7. H-plane beamwidth analysis. (a) Model. (b) HPBW results.

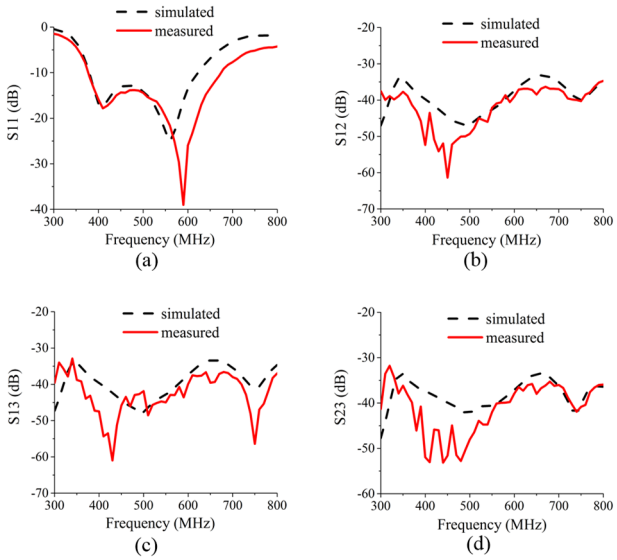

Fig. 8. Simulated and measured S-parameters. (a) S_{11}. (b) S_{12}. (c) S_{13}. (d) S_{23}.

better than 15 dB, thus the neighboring units will generate a large unacceptable interference level.

Further analysis is carried out for clarifying the impact of the rod3 radius on the isolation level in Fig. 6(c), as well as the impact of the rods on the overall antenna performances as shown in Fig. 6(d)–(f). In terms of rod3 radius, a trade-off between isolation level and weight should be achieved, thus the value of 23 mm is used in the final design. Moreover, the results in Fig. 6(d)–(f) demonstrate the effectiveness of rod3 in terms of gain, half-power beamwidth (HPBW), and back-lobe suppression, whereas rod1 and rod2 have a similar impact on the radiation performances. Rod1 is always vertical and at a fixed position, whereas rod2 can be rotated with the WHEMS as an entire unit in the case that the main lobe in the vertical direction should be tilted when this design is applied to base station applications. If a relatively large tilt angle is required, rod2 can be moved farther from rod1 to avoid their mechanical interference without degrading any of the antenna performances.

Further analysis is carried out to demonstrate the flexibility of the proposed design for controlling the beamwidth amplitude. The folded portion of the WHEMS is characterized by a 90° angle; it is bent such that the angle is increased by θ, as shown in Fig. 7(a). The analysis is limited to $\theta = 40°$ to keep the isolation level below -30 dB. The vertical beamwidth, instead, can be easily reduced for applications to base stations by vertically stacking more than one of the proposed units [24]. This will inherently lead to a gain increase, thus making the proposed design suitable for base station applications.

TABLE I
ANTENNA PERFORMANCE COMPARISON

Ref.	BW	S12 (dB)	F/B (dB)	Size ($r\times r$)	Wind load
[24]	52.3%	—	—	$0.35\times0.35\lambda_L^2$	High
[25]	44.5%	30	24	$0.57\times0.57\lambda_L^2$	High
This work	55%	36	>19.7	$0.41\times0.41\lambda_L^2$	Low

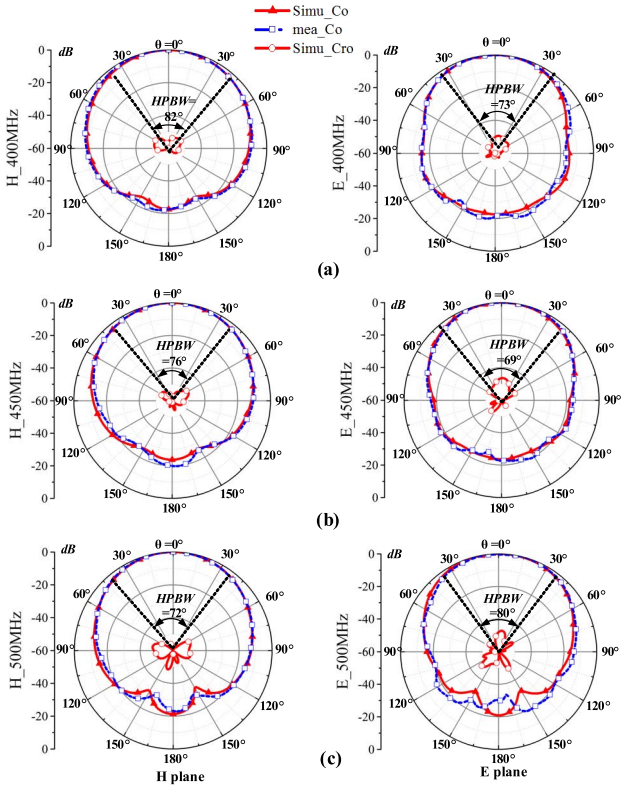

Fig. 9. Simulated and measured patterns in H-plane (xoz plane) and E-plane (yoz plane). (a) 400 MHz. (b) 450 MHz. (c) 500 MHz.

IV. SIMULATION AND REAL TESTING

The measured and simulated S-parameters are shown in Fig. 8. From Fig. 8(a), it can be seen that the measured bandwidth is wider than the simulated one, and the range of measured $|S_{11}| < -10$ dB is 380–670 MHz (55%). From Fig. 8(b)–(d), it can be seen that the measured and simulated curves of S_{12}, S_{13}, and S_{23} are very close to each other, as expected due to the symmetry of the structure. The antenna isolation is greater than 36 dB in the full bandwidth identified above (380–670 MHz), as a consequence of the optimization of the common rod position and length from the parametric analysis in Section III-C. Moreover, the isolation is greater than 40 dB in the 400–500 MHz operating band, such that the influence of adjacent antennas can be completely neglected. The designed antenna achieves high isolation in a compact structure, and it is able to reduce the mutual interference between units. As can be seen from Table I, the present design achieves higher isolation in a smaller grouping radius (r) compared with the antenna in [25].

The test of patterns was performed in the anechoic chamber, comparing the simulation and test results at 400, 450, and 500 MHz, as shown in Fig. 9. The simulated and experimental results of each

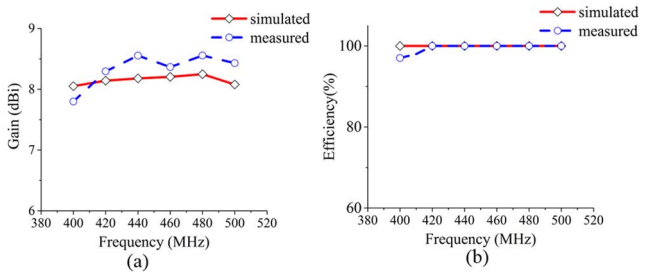

Fig. 10. (a) Gain. (b) Efficiency.

TABLE II
LOW-FREQUENCY ANTENNA APPLICATIONS

Ref.	Bandwidth (MHz)	Gain (dBi)	H/E plane HPBW	F/B ratio (dB)
[6]	400-480	6	85°/120°	15
[7]	470-520	9	65°/60°	18
[8]	403-430	8.1	105°/65	16
This work	400-500	8	75°/72°	19

unit tested in the array agree well with each other. The H-plane HPBW of the antenna units are all greater than 70°, and the E-plane HPBW of the antenna units are greater than 69°. The antenna simulation front-to-back ratio is greater than 20 dB (the worst value from the experimental test is found for the 450 MHz, to be 19.7 dB). The high front-to-back ratio can reduce the interference of the back lobe to other antennas. This work has the advantages of wide bandwidth and high front-to-back ratio compared with other solutions for 400–500 MHz vertical polarization antennas reported in Table II. The simulated cross-polarization is very low in this design, the cross-polarization is lower than −38 dB, and the polarization purity is more than 46 dB. As shown in Fig. 10(a), the simulated gain of the antenna is 8.15 ± 0.12 dBi in 400–500 MHz, whereas the measured gain is 8.2 ± 0.4 dBi. As shown in Fig. 10(b), the simulated and measured efficiency is close to 100%. This design uses an all-metal design, no dielectric loss, low metal loss, good voltage standing wave ratio (VSWR), and low return loss, thus, the antenna is characterized by high efficiency.

V. CONCLUSION

A three-sector linear array antenna for 400–500 MHz is proposed with common metal rod reflectors to decouple adjacent units. The specific design proposed combines the effect of the common rod and the bent of the driving element such that the mutual coupling is minimized by reducing the distance of the common rod from the array center, thus reducing the overall array size. The antenna uses bent driving elements and metal rods to achieve a compact design, thus reducing wind load and manufacturing costs, since only the WHEMS driving element may be required to be encapsulated into a waterproof housing. The design of the array unit and sector array is described in detail, and the decoupling principle of the metal rod structure is analyzed by an extensive parametric analysis. The experimental results, in good agreement with the predicted performances by full-wave simulations, show that the S_{11} is less than −10 dB in the range of 380–670 MHz (55%). The H-plane HPBW is greater than 70°, with a front-to-back ratio greater than 19 dB. The isolation is greater than 40 dB, and a stable gain of 8.2 ± 0.4 dBi is obtained in the 400–500 MHz. The array adopts an all-metal structure, with unit spacing less than 0.2λ, low wind load, and high isolation, and

can be used for CBD data communication and residential subdivision applications. The proposed decoupling method has the potential to be implemented into the design of dual-polarized decoupling parasitic elements, which helps to achieve a compact design for low-frequency dual-polarized base station antennas.

REFERENCES

[1] R. T. Caldeira, D. C. Melgarejo, and R. Coutinho, "Application of LTE 450 MHz in the electric energy sector," in *Proc. Eur. Conf. Netw. Commun. (EuCNC)*, Oulu, Finland, Jun. 2017, pp. 1–5.

[2] Y. Niu, J. Ding, D. Fei, Z. Zhong, and Y. Liu, "Doppler effect on high-speed railway at 465 MHz," in *Proc. IEEE Int. Symp. Antennas Propag. USNC-URSI Radio Sci. Meeting*, Atlanta, GA, USA, Jul. 2019, pp. 2117–2118.

[3] A. A. Antonov, I. K. Surin, M. S. Karpovich, and D. L. Shlemin, "A high gain 450/900 MHz dual band low noise amplifier for IoT and LTE low-band receivers," in *Proc. 20th Int. Conf. Young Spec. Micro/Nanotechnol. Electron Devices (EDM)*, Erlagol, Russia, Jun. 2019, pp. 92–96.

[4] I. Bobkov, A. Rolich, M. Denisova, and L. Voskov, "Study of Lora performance at 433 MHz and 868 MHz bands inside a multistory building," in *Proc. Moscow Workshop Electron. Netw. Technol. (MWENT)*, Moscow, Russia, Mar. 2020, pp. 1–6.

[5] C. Jiajia and L. Mingming, "Coexistence analysis between eMTC and LTE-R/broadcasting service system in 450 MHz–470 MHz band," in *Proc. IEEE 2nd Int. Conf. Inf. Commun. Signal Process. (ICICSP)*, Weihai, China, Sep. 2019, pp. 15–19.

[6] Guangxi Routon Technology. (Aug. 2021). *The FTD-04PB06V90 Planar Antenna*. [Online]. Available: http://en.gxjinglun.com/index.php?a=shows&catid=174&id=253

[7] Guangxi Routon Technology. (Aug. 2021). *The FTD-04PB09V65 Planar Antenna*. [Online]. Available: http://en.gxjinglun.com/index.php?a=shows&catid=174&id=255

[8] Sinclair Technologies. (Aug. 2021). *SY303-SF1SNM(ABK)*. [Online]. Available: https://www.sinctech.com/collections/base-station-antennas/products/yagi-ant-6-dbd-black-anodized-403-430-mhz

[9] Q. Yuan, Q. Chen, and K. Sawaya, "Performance of adaptive array antenna with arbitrary geometry in the presence of mutual coupling," *IEEE Trans. Antennas Propag.*, vol. 54, no. 7, pp. 1991–1996, Jul. 2006.

[10] R. Janaswamy, "Effect of element mutual coupling on the capacity of fixed length linear arrays," *IEEE Antennas Wireless Propag. Lett.*, vol. 1, pp. 157–160, 2002.

[11] A. Diallo, C. Luxey, P. Le Thuc, R. Staraj, and G. Kossiavas, "Enhanced two-antenna structures for universal mobile telecommunications system diversity terminals," *IET Microw., Antennas Propag.*, vol. 2, no. 1, pp. 93–101, Feb. 2008.

[12] C.-Y. Chiu, C.-H. Cheng, R. D. Murch, and C. R. Rowell, "Reduction of mutual coupling between closely-packed antenna elements," *IEEE Trans. Antennas Propag.*, vol. 55, no. 6, pp. 1732–1738, Jun. 2007.

[13] M. Ayatollahi, Q. Rao, and D. Wang, "A compact, high isolation and wide bandwidth antenna array for long term evolution wireless devices," *IEEE Trans. Antennas Propag.*, vol. 60, no. 10, pp. 4960–4963, Oct. 2012.

[14] C.-H. Wu, C.-L. Chiu, and T.-G. Ma, "Very compact fully lumped decoupling network for a coupled two-element array," *IEEE Antennas Wireless Propag. Lett.*, vol. 15, pp. 158–161, 2016.

[15] B. C. Pan and K. J. Cui, "Broadband decoupling network for dual-band microstrip patch antennas," *IEEE Trans. Antennas Propag.*, vol. 65, no. 10, pp. 5595–5598, Oct. 2017.

[16] K.-L. Wu, C. Wei, X. Mei, and Z.-Y. Zhang, "Array-antenna decoupling surface," *IEEE Trans. Antennas Propag.*, vol. 65, no. 12, pp. 6728–6738, Dec. 2017.

[17] Y. Qi, L. Zhu, X. Chen, and W. Wang, "Wideband slot-loop antennas for wireless communication systems," U.S. Patent 2 263 055 A1, Sep. 5, 1999.

[18] L. Chi *et al.*, "Rugged linear array for IoT applications," *IEEE Internet Things J.*, vol. 7, no. 6, pp. 5078–5087, Jun. 2020.

[19] L. Chi, Y. Qi, Z. Weng, W. Yu, and W. Zhuang, "A compact wideband slot-loop directional antenna for marine communication applications," *IEEE Trans. Veh. Technol.*, vol. 68, no. 3, pp. 2401–2412, Mar. 2019.

[20] L. Chi, Y. Qi, Z.-B. Weng, W. Yu, F. Li, and J. L. Drewniak, "Directional antenna with consistent H-plane dual-band beamwidth for Wi-Fi applications," *IEEE Trans. Antennas Propag.*, vol. 67, no. 7, pp. 4495–4505, Jul. 2019.

[21] L. Chi, Z. Weng, Y. Qi, and J. L. Drewniak, "A 60 GHz PCB wideband antenna-in-package for 5G/6G applications," *IEEE Antennas Wireless Propag. Lett.*, vol. 19, no. 11, pp. 1968–1972, Nov. 2020.

[22] Y. Xiao, Y. Qi, F. Li, J. Fan, W. Yu, and L. Lu, "Dual-band directional slot antenna for Wi-Fi application," *IEEE Trans. Antennas Propag.*, vol. 66, no. 8, pp. 4277–4281, Aug. 2018.

[23] J. D. Kraus and R. J. Marhefka, "End-fire antenna: The helical beam antenna and the Yagi–Uda array. Part I," in *Antennas For All Applications*, 3rd ed., Y. Yu, Eds. Beijing, China: Publishing House of Electronics Industry, 2008, pp. 242–246.

[24] L. H. Ye, Y. F. Cao, X. Y. Zhang, Y. Gao, and Q. Xue, "Wideband dual-polarized omnidirectional antenna array for base-station applications," *IEEE Trans. Antennas Propag.*, vol. 67, no. 10, pp. 6419–6429, Oct. 2019.

[25] J.-S. Row and C.-W. Tsai, "A three-sector array with switchable beams," *Microw. Opt. Technol. Lett.*, vol. 59, no. 6, pp. 1357–1361, Jun. 2017.